

Response of the air flow energy harvester with two side-by-side bluff-bodies of various shapes

Syed Amjad Ahmed¹, Grzegorz Litak², Mateusz Waśkowicz^{2*},
Dineshkumar Ravi², Abhijeet M. Giri², Jacek Caban²

¹ C. Abdul Hakeem College of Engineering and Technology, 632509 Vellore, India

² Faculty of Mechanical Engineering, Lublin University of Technology, Nadbystrzycka 36, 20-618 Lublin, Poland

* Corresponding author's e-mail: m.waskowicz@pollub.pl

ABSTRACT

The experimental results of flow energy harvesting where the bluff-bodies with different shapes of cross-section are mounted at the ends of the cantilever beams were presented. Namely, bluff-bodies – as cylinders and rectangles – were considered for the interaction with flowing air. The bluff-bodies are coupled through the joint suspension frame where the other cantilever ends were clamped and coupled additionally by vortices created in the space between them. Finally, piezoelectric patches with corresponding electrical circuits were attached to the cantilever beams. They transduce the mechanical energy of the beam-bluff-body resonators into the electrical power. The resulting structure oscillated interacting with the airflow with a range of velocities. High amplitude oscillations caused by the interaction of vortices produced larger voltage response in the electric circuits. As the bluff-bodies of different shapes respond differently, moderate voltage output over a wider velocity range was observed. For illustration of the energy transduction mechanism and qualitative validation of the experimental results, numerical simulations were performed. The differences in the vortex formation and shedding responsible for the vibrations induced in the mechanical structure were shown.

Keywords: alternative energy, bluff-bodies, computational fluid dynamics, energy harvesting.

INTRODUCTION

The issues of energy demand, production and optimization of energy consumption and its saving are the subject of many scientific and research works (Gnap et al., 2020; Hurtova et al., 2018; Jereb et al., 2021; Małek et al., 2023). The structure of energy demand in the Polish economy and investments in the energy sector are presented in (Derkacz and Dudziak, 2021). In many countries, work is currently underway to transform energy by moving away from coal in favor of energy from renewable sources, including the share of wind (Michael et al., 2021; Piotrowska et al., 2022) and solar energy (Ghazouani et al., 2025; Kettle et al., 2022; Kilikevičienė et al., 2019), as well as hydropower (Jadon et al., 2020; Đurin et al., 2022; Thapa et al., 2022). Furthermore, there is a visible increase in interest in development

of alternative fuels for the automotive industry, such as biomass (Kantová et al., 2021; Szyszlak-Bargłowicz et al., 2018; Trnka et al., 2021) or bio-fuels (Adalieh 2022; Gis et al., 2016; Norhafana et al., 2019). As it can be seen, the modern world is characterized by a high demand for energy sources in every form as well as in every sector of the economy and human life, including suppliers of small portable electronic devices and systems for monitoring the condition of structures. Due to the growing demand for energy, there has been an increased interest in various technical systems to reduce its consumption (Farghali et al., 2003) and to obtain energy from the environment (Yu et al., 2024). Among the various energy sources, mechanical vibrations have also been considered (White et al., 2001; Mitcheson et al., 2008; Erturk et al., 2009; Borowiec 2015; Nowak and Pietrzakowski 2016; Yang et al., 2018; Ma et al., 2018).

Corresponding energy harvesting devices usually consist of a mass resonator coupled with an appropriately selected piezoelectric transducer to keep the higher energy transduction efficiency (Yang et al., 2018). Usually, the frame with the resonator is excited kinematically to mimic the influence the surrounding environment under laboratory testing conditions by inducing harmonic vibrations in the assumed frequency range (frequency sweep) (Ma et al., 2018). To obtain the best effects, the piezoelectric transducer is placed along the most flexible part of the cantilever beam. Finally, the electrodes connect the piezoelectric patches to an electrical circuit providing an electromotive force induced as a result of the beam deformation. It was checked that such a system works well in the resonant region of the mechanical structure (White et al., 2001; Mitcheson et al., 2008). Unfortunately, in the case of environmental conditions (wind, sea waves or vehicle traffic) that are characterized by high variability in the frequency and amplitude, the amount of energy harvested is not sufficient. This limitation was removed by application of nonlinear effects (Cottone et al., 2009; Friswell et al., 2012; Daqaq et al., 2014; Zhou et al., 2018).

Wind induced mechanism leading to vibration of mechanical resonator was also under study by last few years (Ma and Zhou 2022; Wang et al., 2020; Zhang et al., 2023). Especially, the mechanism of vortex induced vibration and galloping effect were present for various bluff-body shapes and air flow velocities (Wang et al., 2020). Nonlinear interaction between air flow and bluff-body lead to creation of vortices and eddies and a frequency lock phenomenon (Zhang et al., 2023). Two side-by-side cylinders arrangement was discussed elsewhere (Munir et al., 2017; Irawan et al., 2023; Weilin et al., 2019); however,

combinations of different cross-sectional shapes, mechanical couplings and mistuning were not investigated. Furthermore, the piezoelectric coupling was not present in these studies.

In this study, the experimental results were presented for the flow energy harvesting, where the two bluff-bodies with different shapes of the cross-section were placed at the ends of the cantilever beams in the side-by-side arrangement. Two piezoelectric material patches, one on each beam, were bonded for transduction of mechanical strain into the electrical output. This investigation was aimed at finding out the better combination of bluff-body cross-sections, which produces enough dynamical response for piezoelectric energy harvesting. The testing structure oscillated on the flowing air with several flow velocity ranges. For illustration of the energy transduction mechanism and qualitative validation of the experimental results, Computational Fluid Dynamics (CFD) simulations were performed. Owing to these, it is possible to show the differences in the formation and shedding of vortices that cause vibration of experimental mechanical structure in simulated various environmental conditions.

EXPERIMENTAL ANALYSES

Description of the experimental setup

In order to analyse the oscillations of the two bluff-bodies of various cross-sections, a side-by-side arrangement of the two cantilevered beams attached with the piezoelectric elements is mounted in the HM 170 open-type wind tunnel (GUNT Hamburg). Such an arrangement is shown in Figure 1a. An enlarged view as shown

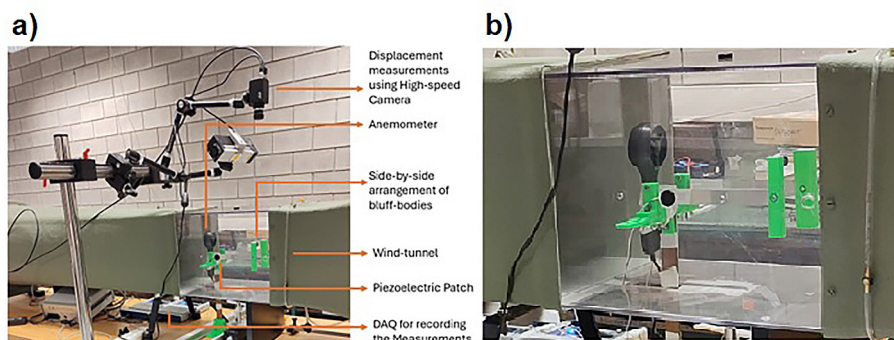


Figure 1. Experimental arrangement of the two side-by-side beam oscillators is shown here with the description of components and orientation of the system with respect to the wind-flow (b) A magnified view of circular-square combination of the two bluff-bodies

in Figure 1b presents further details. More details about the wind-tunnel can be found in (Ambrozkiewicz et al., 2021; Ambrozkiewicz et al., 2022; Ambrozkiewicz et al., 2024).

The system parameters and details of cylinder configurations are included in Table 1. Additionally, length of the bluff-bodies is 100 mm, the length, width, and thickness of beams are 170 mm, 20 mm and 0.6 mm, respectively. The center-to-center gap between the two beams was maintained at 81.5 mm. The free stream flow velocity (in m/s) is considered over a range of 3.5 to 10 m/s. The linear spring constant for the beam was computed as 46.16 N/m.

The voltage signals from the piezoelectric elements attached to the beam, at various air flow rates, for the geometries mentioned in Table 1 are obtained using NI-UX4351 data acquisition system. The reduced velocity denote ratio of wind velocity divided by the natural frequency of the mass-spring system and the diameter of the bluff-body. The air flow rates are measured using a digital anemometer mounted behind the side-by-side

arrangement, as shown in Figure 1. By varying the air flow rates through the wind tunnel, the voltage signals are recorded for 10 minutes. The NI-DAQ card has data acquisition limitation of +10 to -10 V; hence signals recorded beyond this range are truncated.

RESULTS

For the experiments, the sequential cases of configurations from Table 1 were used. The corresponding voltage outputs are presented in Figures 2–5 and the corresponding Tables. Figure 2 shows the voltage results of two bodies (S-S) of Case 1 configuration. The red curve denotes the piezoelectric voltage from the right-side beam and it is shifted up on the graph by the 1V level flow, while the blue plot represents the left beam and denotes the left beam piezoelectric voltage. The discrepancy between the amplitude are caused by the small mistuning of the beams (Table 1) and the dynamical effect of multiple asymmetric

Table 1. Details of cylinder configurations

Sr. No	Bluff-body combination	Mass (gms)	Natural frequency of beam-mass system (f, Hz)	Aspect ratio (L/D)	Reduced velocity U^*	Reynolds number
Case-1 (S-S)	Squares (21 mm side)	R-10.16 L-10.12	R-10.73 L-10.75	4.76	15-45	5000–14000
Case-2 (C-S)	R- circular (21 mm dia.) L- square (21 mm side)	R-8.03 L-8.09	R-12.07 L-12.08	4.76	15-45 13-40	5000–14000
Case-3 (CH-CH)	Circular – hollow (30 mm dia.)	R-13.57 L-13.70	R-9.29 L-9.24	3.33	13-36	6900–19000
Case-4 (V-V)	Variable (22 mm dia. on top side and 20 mm square on bottom side)	R-15.35 L-15.46	R-8.73 L-8.70	4.54	18-52	5000–14500

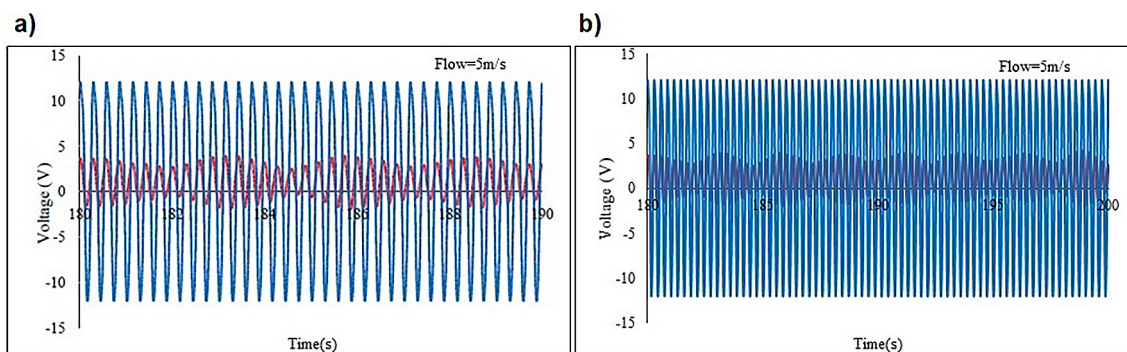


Figure 2. Case-1 Square-Square combination (S-S). Induced voltages from the piezoelectric patches are shown (a) for 10 sec and (b) for 20 sec

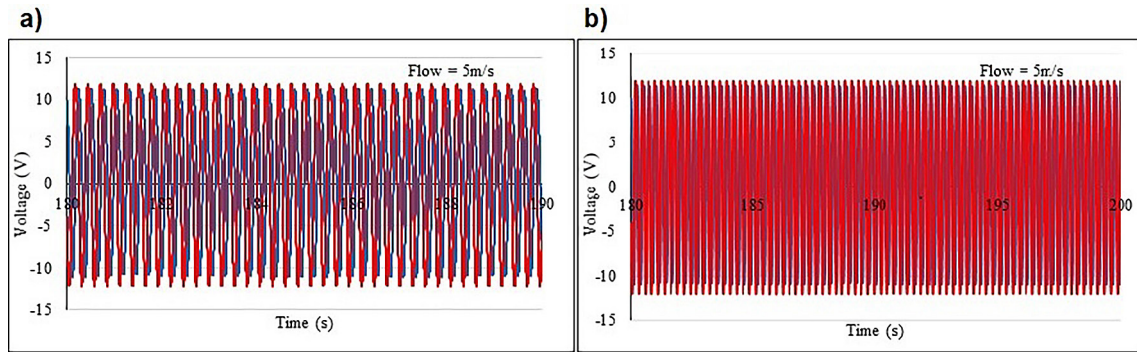


Figure 3. Case-3 Cylinder-Square combination (C-S). Induced voltages from the piezoelectric patches are shown (a) for 10 sec and (b) for 20 sec

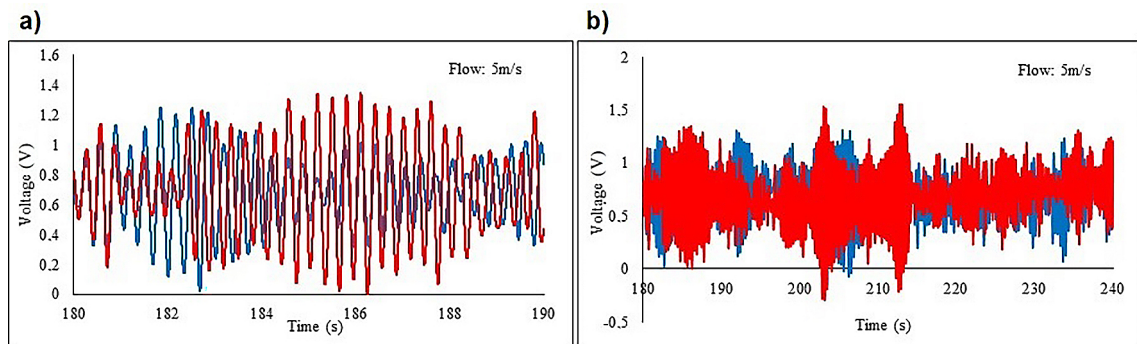


Figure 4. Case-3 hollow cylinder- hollow cylinder combination (CH-CH). Induced voltages from the piezoelectric patches are shown (a) for 10 sec and (b) for 60 sec. Note that the voltage oscillations are going around the 0V level, but it is not kept in the figures

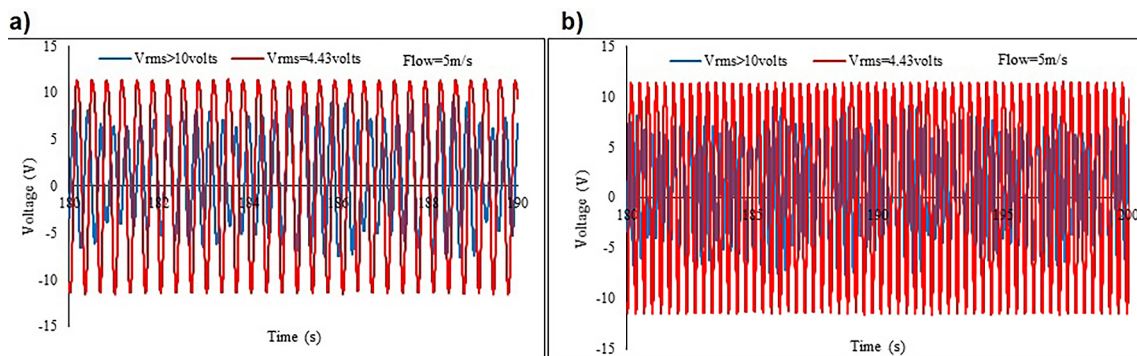


Figure 5. Case-4 two prismatic bluff-bodies with circular shape at top and square shape at the bottom combination (V-V). Induced voltages from the piezoelectric patches are shown (a) for 10 sec and (b) for 20 sec

solutions. Table 2 summarizes the results from Figure 2 for various air speeds. For all the wind speeds, the left beam piezoelectric voltage is higher signalling that the displacement oscillations of the left beam are of higher amplitude with respect to the right beam.

In Figure 3, the results of voltage outputs for the harvester with circular – square cross-sections were presented. In this case, the Left and right beams results are balanced. The results show

periodic responses. On the other hand, Figure 4 indicates the corresponding voltage results for the system of two hollow cylinders. Here, the oscillations are of much smaller range and they are evidently nonperiodic. Interestingly, these voltage oscillations and simultaneous beam vibrations are not balanced in the amplitude, but their maximum is passing from one beam to another with evolving time. It seems to be an alternative exchange of energy through a coupling of fluid medium.

Table 2. RMS voltages at different reduced velocities for the Case -1 S-S. The sign > is used to indicate the large scale oscillations beyond the measurement range

Flow velocity (m/s)	Voltage (V)			
	R		L	
	Vrms	Vpeak	Vrms	Vpeak
4	2.51	4.64	>10	>10
5	>10		2.00	4.75
6			0.98	6.02
7			2.96	8.07
8			0.82	9.03
9			5.49	>10

Finally, the results for the system composed of two prismatic bluff-bodies with a circular shape at the top and square shape at the bottom (V-V) are studied. The results are presented in Figure 5 and summarized for various air flow velocities in Table 3. Here, the results indicate the right beam (red color) dominance over the left one (blue color). This effect was presumably due to the small mistuning and possibilities of two or more asymmetric solutions.

General observations

The following are some of the general observations made during the experiments.

1. The bluff-bodies (for all the cases) initially vibrate with the torsional vibrations, and finally results in the transverse oscillations. In particular, with the square shapes, the torsional vibration persists for larger periods before its transition into the transverse oscillations.
2. When the oscillations are established, either of the beam, depending on the flow velocity, produces higher amplitude of oscillations. Such a behavior may be attributed to the mistuning of the beams and the air flow across the cylinders.
3. Nevertheless, for the square-circular (C-S)

arrangement, the oscillations are found to be steady periodic and of a large amplitude. As it was observed earlier, the torsional vibrations are enhanced in the square cylinder compared to that of the circular cylinder. The oscillations in the square shape start prior to that of the circular cylinder (Fig. 3). Accordingly, the displacement of the beam with the circular cylinder, in the C-S case, is found to be higher than that obtained for the other cases.

4. In most of the cases, except for Case-2, unbalanced (or asymmetric) solutions were found with one bluff-body larger in activities. Interestingly, Case-4 produced different results where the higher excitation amplitude of the beams was exchanged by the two beams alternatively with time.

Remarks and conclusions on the experimental observations

The following remarks can be made based on the experimental observations:

1. The reduced velocities in the present experiments are significantly different from the ones expected for the vortex-induced vibrations.
2. Among the cylinder configurations considered

Table 3. RMS voltages at different reduced velocities for the Case-5 V-V

Flow velocity (m/s)	Reduced velocity	Voltage (V)			
		R		L	
		Vrms	Vpeak	Vrms	Vpeak
4	20.86	>10		3.30	3.88
5	26.07			4.43	8.83
6	31.28			4.36	8.96
7	36.50			>10	
8	41.71				
9	52.13				

in the present experimentation, the square-square (S-S) and square-circular (C-S) arrangements provide enhanced oscillations and voltage output.

3. The torsional mode of vibrations is generally observed in all the cases; however, the torsional vibrations are greater in amplitude for the square-shaped bodies.
4. At higher flow rates, the mutual hitting of the bluff-bodies can be avoided by increasing the span between the cylinders or by installing stoppers. These solutions will add further non-linear effects. However, increasing the span between the cylinders may possibly be restricted by the walls of the wind tunnel test section.

NUMERICAL SIMULATION EXAMPLES

In order to establish qualitative validation and similarities, numerical simulations of a few cases of bluff-body combinations were performed. In this section, the results of computational fluid dynamics (CFD) simulations performed using ANSYS (vR23) software are presented. The fluid structure interaction motion of the bluff-body is

assumed to take place only in the transverse direction to the wind-flow. Thus, the linear stiffness (46.16 N/m) of the cantilever beam is considered to offer the restoring force to the lift forces exerted by the fluid on the bluff-body. It is assumed that mass (10 gms) of all the bluff-bodies remains same irrespective of the shape and the orientation with the direction of the wind-flow. Also, the hydraulic diameter and length of the bluff-bodies are considered to be 21 mm and 100 mm, respectively. Two side-by-side bluff-bodies are separated with a distance of 3 times the hydraulic diameter (Weilin et al., 2019).

The computational domain considered for the CFD simulations is shown in Figure 6a, in which the inner and outer domains are highlighted. Block meshing strategy is used for better implementation of boundary conditions. Mesh instances around the circular and square shapes of the bluff-bodies are also shown in Figure 6b. These meshes are built using the O-grid technique to maintain the smooth transition of element sizes, so as to maintain consistent higher quality of mesh and capture precisely the developed patterns of the vortices. Table 4 describes the boundary conditions used at different locations in the

Table 4. Description of the boundary conditions used for the numerical simulations

Sr. No.	Boundary	Type	Specified conditions
1	Inlet – outer and Inner domains	Velocity Inlet	0.5 to 4.0 (m/s)
2	Top wall	Symmetry	Symmetry
3	Bottom wall	Symmetry	Symmetry
4	Outlet	Pressure outlet	1 Bar
5	Inner domain – top, bottom, and Back end	Interface	Interface

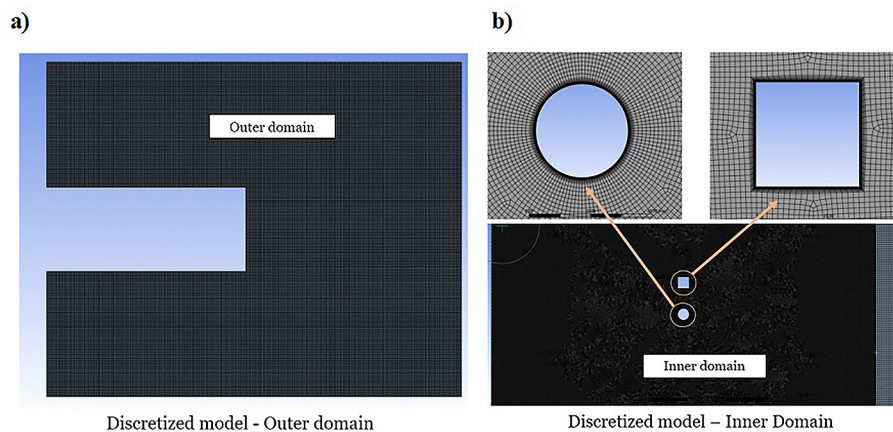


Figure 6. (a) Details of the computational domain and meshing scheme used for the numerical simulations are shown here, (b) O-grid meshing used around the bluff-bodies is shown in the exaggerated views

mesh domain. Although several wind speeds ranging from 0.5 – 4.0 m/s are used in numerical simulations, the results obtained at 3 m/s of wind speed were presented to compare various combinations of the bluff-bodies.

Mathematical modelling and solution technique

A two-dimensional simplified model of a beam integrated with the bluff-body has been solved numerically through finite volume approach using ANSYS Fluent 23.2 commercial CFD code. The fluid flow variations across various bluff-body shapes were simulated by solving the governing equations (Anderson et al., 2013), namely, conservation of mass (Eq. 1) and momentum (Eq. 2a–b). The turbulence induced in the flow has been captured by solving the Shear Stress Transport (SST) $k-\omega$ model of closure.

$$\frac{\partial u}{\partial x} + \frac{\partial v}{\partial y} = 0 \tag{1}$$

Scalar momentum equation of velocity component in x direction is given by:

$$\begin{aligned} \frac{\partial u}{\partial t} + u \frac{\partial u}{\partial x} + v \frac{\partial u}{\partial y} = & -\frac{1}{\rho} \frac{\partial p}{\partial x} + \\ & + \vartheta \left(\frac{\partial^2 u}{\partial x^2} + \frac{\partial^2 u}{\partial y^2} \right) - \frac{\partial \tau_{txx}}{\partial x} - \frac{\partial \tau_{txy}}{\partial y} \end{aligned} \tag{2a}$$

The scalar momentum equation of the velocity component in the y-direction is given by:

$$\begin{aligned} \frac{\partial v}{\partial t} + u \frac{\partial v}{\partial x} + v \frac{\partial v}{\partial y} = & -\frac{1}{\rho} \frac{\partial p}{\partial y} + \\ & + \vartheta \left(\frac{\partial^2 v}{\partial x^2} + \frac{\partial^2 v}{\partial y^2} \right) - \frac{\partial \tau_{tyx}}{\partial x} - \frac{\partial \tau_{tyy}}{\partial y} \end{aligned} \tag{2b}$$

where: $\vartheta = \frac{\mu}{\rho}$.

Next, the turbulent kinetic energy k of the standard $k-\omega$ two-equation turbulent model is given by Eqs. 3(a–b). The turbulent dissipation rate “ ω ” is given by Eq. 3b.

$$\begin{aligned} \frac{\partial k}{\partial t} + u \frac{\partial k}{\partial x} + v \frac{\partial k}{\partial y} = & \frac{\partial}{\partial x} \left[(\vartheta + \sigma_k \vartheta_t) \frac{\partial k}{\partial x} \right] + \\ & + \frac{\partial}{\partial y} \left[(\vartheta + \sigma_k \vartheta_t) \frac{\partial k}{\partial y} \right] + P_k - \beta \rho k \omega \end{aligned} \tag{3a}$$

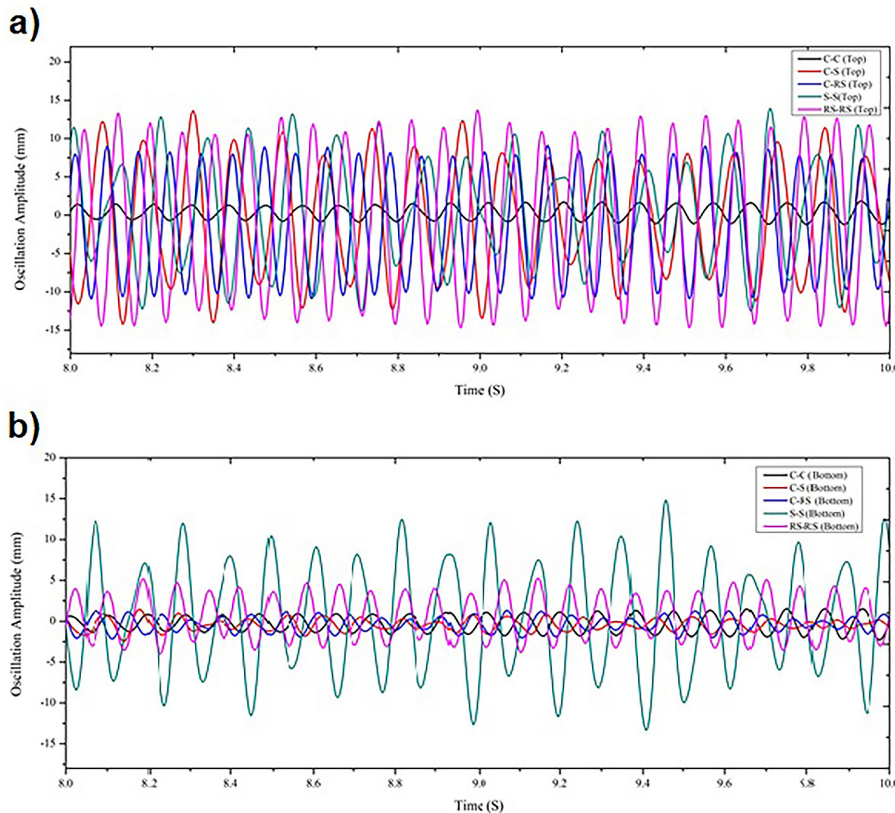


Figure 7. Time histories of the transverse displacement amplitudes of the bluff-bodies at (a) top and (b) bottom position. Different colors of the plots correspond to the combinations of the bluff-bodies mentioned in the legends.

$$\frac{\partial \omega}{\partial t} + u \frac{\partial \omega}{\partial x} + v \frac{\partial \omega}{\partial y} = \frac{\partial}{\partial x} \left[(\vartheta + \sigma_{\omega \vartheta_t}) \frac{\partial \omega}{\partial x} \right] + \frac{\partial}{\partial y} \left[(\vartheta + \sigma_{\omega \vartheta_t}) \frac{\partial \omega}{\partial y} \right] + \alpha \frac{\omega}{k} P_k - \beta \rho \omega^2 \quad (3b)$$

The turbulent viscosity (μ_T) is expressed as $\mu_T = \rho \frac{k}{\omega}$. The governing equation of motion for the structural side without including the damping term can be given by Eq. (4) below.

$$m\ddot{x} + kx = F_l(t) \quad (4)$$

where: the lift coefficient $C_l(t)$ is used to estimate the lift force $F_l(t) = \frac{1}{2} \rho A U^2 C_l(t)$.

In Figure 7, steady-state time histories of transverse displacement oscillations of the bluff-bodies are presented for the five combinations of the shapes of the bluff-bodies. These combinations are mentioned in the legends of Figure 7(a–b) and are referred to as circular-circular (C-C), circular-square (C-S), circular-rotated square (C-RS), square-square (S-S), and square-rotated square (S-RS). The physical orientation of these bluff-body combinations can be visualized in the corresponding Figures 8(a–b), Figures 9(a–b), and Figure 10, respectively. Figures 8 to 10 show the patterns of the vortices induced due to the wind interactions with the beam structures.

In Figure 8, for the case C-C shown by the black lines, both the bluff-bodies can be observed

to oscillate with a similar amplitude and frequency. This is because the vortex shredding pattern, shown in Figure 8a, shows the non-mixing nature of the vortices, suggesting no influence on the motion of each other. As the upper body is replaced by a square in the C-S case shown in Figure 8b, it can be seen that the oscillations of the lower circular bluff-body are influenced and become irregular and aperiodic. The square-shaped bluff-body shreds larger vortices with eddies that interact with the circular bluff-body causing such aperiodic oscillations of the later one. It is known from the literature that square-shaped bluff-bodies operate with the combination of VIV and galloping (Zhao et al., 2013), and hence produce large amplitude of oscillations. When the upper body is replaced by a rotated-square shape in the C-RS case (Figure 9a), the influence on the circular bluff-body is similar to the previous case with aperiodic oscillations of the circular bluff-body. However, the top RS shape seems to enhance the vortex size producing higher lift forces on the upper bluff-body.

In the fourth case S-S, the lower bluff-body is also replaced by a square shape, as shown in Figure 9b. The oscillations of both the bluff-bodies are relatively higher as compared to the C-C, C-S, and C-RS cases, possibly due to the higher contribution from the galloping effects from both the bodies. Even though the C-S case presents the higher amplitude of square-shaped body, the

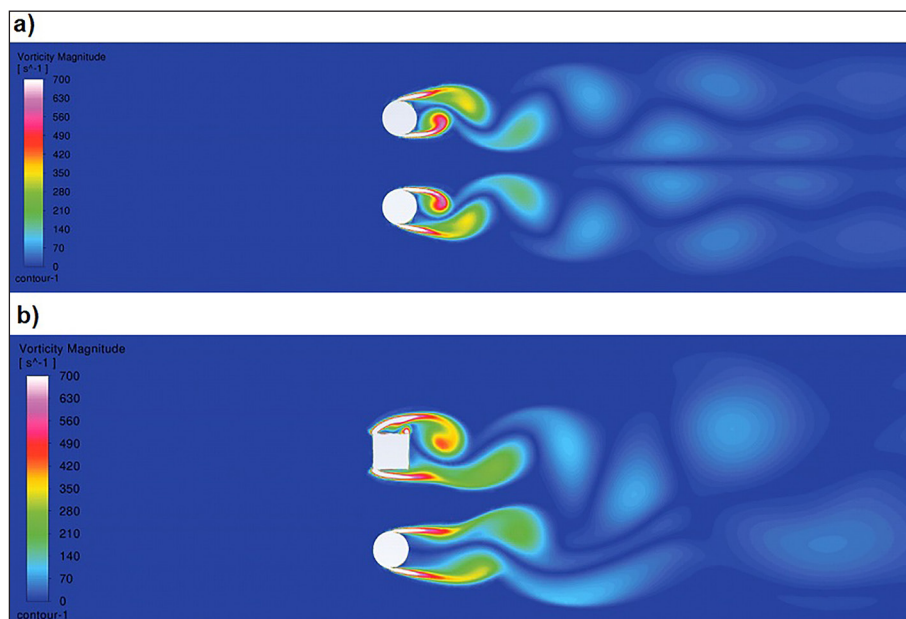


Figure 8. Patterns of induced vortices obtained using the numerical simulations are shown here for the (a) Circular-Circular (C-C) and (b) Square-Circular (C-S) combinations of the bluff-bodies

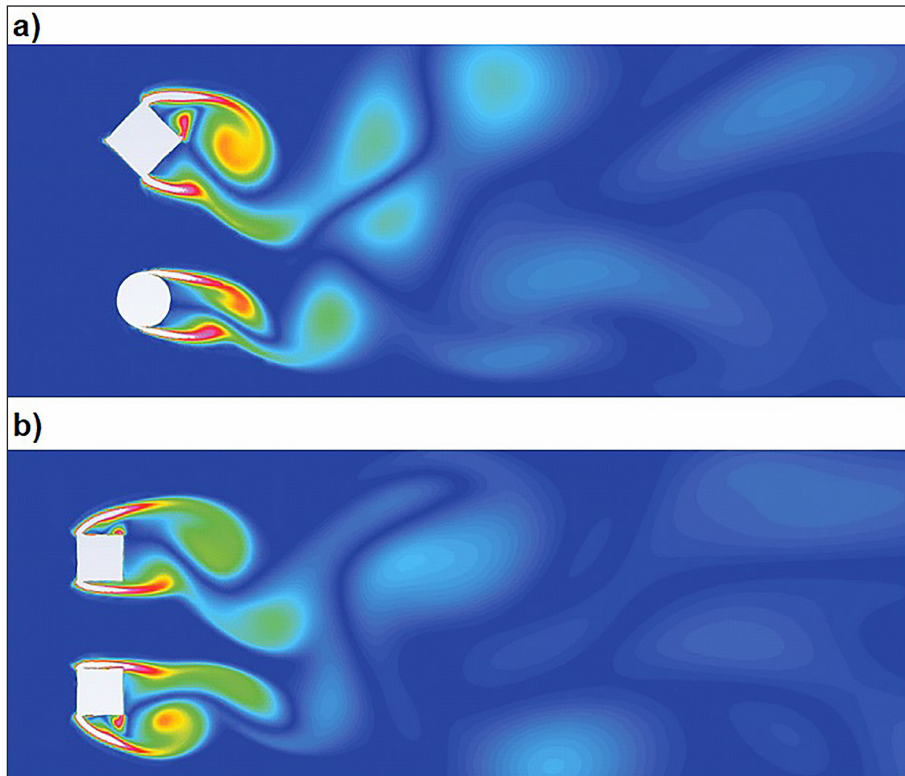


Figure 9. Patterns of induced vortices obtained using the numerical simulations are shown here for the (a) Rotated Square-Circular (RS-C) and (b) Square-Square (S-S) combinations of the bluff-bodies. The magnitude of vorticity can be estimated using the same color scale as show in Figure 8

combined motion with circular-shape is lower in C-S case, which makes the S-S as the most interacting vortex shredding case producing larger oscillations for both the bodies.

In the last case, the upper body is replaced by a rotated-square shape as shown in Figure 10. Compared to the C-RS case, the upper RS shape further produces larger oscillations when paired with the square shape, owing to the stronger interactions and mixing of the vortices shred from both the bluff-bodies. It can be also noticed from the time histories shown in Figure 7, that the frequency of oscillations slightly increases with the introduction of the square and rotated square

shapes. As contribution from the galloping effects build up with the use of square shapes, the aperiodic nature of the oscillations increases. The VIV mechanism of flow interaction seems to build up and sustain for larger wind speeds when the circular shapes are used.

In the numerical simulations, coupling between the two beam structures existed only through the flow interaction, and no other mechanical means of coupling the two structures was considered. However, a weak mechanical coupling between the two beam structures was present through their common connection at the base excitation point. It is observed that such a

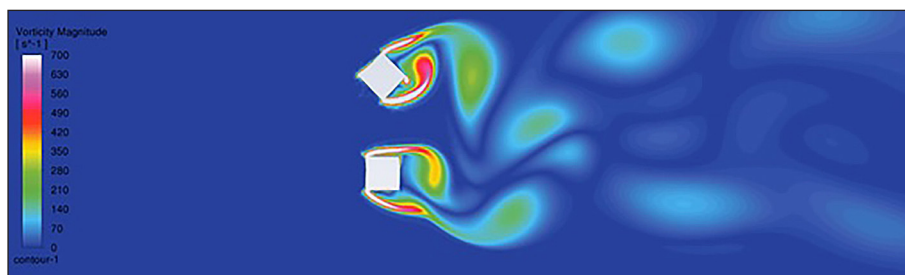


Figure 10. Patterns of induced vortices obtained using the numerical simulations are shown here for the Square-Rotated Square (S-RS) combination of the bluff-bodies

coupling helps in transferring motion as well as initial excitations and influences the oscillations of the two bluff-bodies. In future numerical simulations, such a weak coupling can be simulated using spring or magnetic arrangements.

CONCLUSIONS

The effects of various geometrical shapes of bluff-bodies in the side-by-side arrangement are studied experimentally and numerically. The combinations, namely, cylindrical-cylindrical (C-C), cylindrical-square (C-S), cylindrical-rotated square (C-RS), square-square (S-S) and square-rotated square (S-RS) are considered. Further, experimental investigation on the bluff-bodies with varying cross-section has shown a significantly higher voltage output compared to the configurations with constant cross-sections. The results of the numerical simulations showed that the similar shape combination C-C produced a non-mixing symmetric pattern of vortices with oscillations of relatively small amplitude, but of periodic nature. A noticeable improvement was observed for the C-S case due to the possible presence and interaction of both galloping and VIV mechanisms. A similar trend with further improvement in oscillation amplitudes was observed for the C-RS case. The S-S case provides higher amplitude of oscillations with continuous mixing of vortices, which makes it suitable for energy harvesting purpose. However, uncontrolled and monotonous increments in the amplitudes observed during experiments for such shapes due to galloping at higher operating velocities may damage the piezoelectric elements. The geometric asymmetry in the S-RS case leads towards an uneven pressure distribution and chaotic mixing of vortices, causing the bluff-body to oscillate with highest amplitude among all the cases considered in this investigation. Both the experimental and numerical results have predicted such a behavior with aperiodic oscillations. Such a combination may exhibit widened lock-in region at lower wind speeds and galloping at higher wind speeds. As long as the oscillation amplitudes are regulated, such combinations can improve the effectiveness of these energy harvesting structures. In order to replicate the weak mechanical coupling as observed in the experimental conditions, numerical simulations with

spring or magnetic coupling between the two beam structures can be performed as future tasks.

Acknowledgements

This research was funded by National Science Centre, Poland under the project SHENG-2, No. 2021/40/Q/ST8/00362.

REFERENCES

1. Adailleh, W. (2022). Experimental study of the compression ignition engine performance Using Various Bio Diesel Blends. *Advances in Science and Technology Research Journal*, 16, 29–37. <https://doi.org/10.12913/22998624/151943>
2. Ambroźkiewicz, B., Czyż, Z., Karpiński, P., Stączek, P., Litak, G., Grabowski, Ł. (2021). Ceramic-based piezoelectric material for energy harvesting using hybrid excitation. *Materials*, 14(19), 5816. <https://doi.org/10.3390/ma14195816>
3. Ambroźkiewicz, B., Czyż, Z., Pakrashi, V., Anzarski, J., Stączek, P., Koszewnik, A., Wendeker, M., Litak, G. (2024). Performance assessment of a piezoelectric vibration energy harvester for hybrid excitation with varying cross sections. *Sensors*, 24(23), 7629. <https://doi.org/10.3390/s24237629>
4. Ambroźkiewicz, B., Czyż, Z., Stączek, P., Tiseira, A., García-Tiscar, J. (2022). Performance analysis of a piezoelectric energy harvesting system. *Advances in Science and Technology Research Journal*, 16(6), 179–185. <https://doi.org/10.12913/22998624/156215>
5. Anderson, J.D., Drez, G., Dick, E., Grundmann, R. *Computational fluid dynamics: an introduction*. Springer Science & Business Media, Berlin, Heidelberg, 2013.
6. Borowiec, M. (2015). Energy harvesting of cantilever beam system with linear and nonlinear piezoelectric model. *European Physical Journal: Special Topics*, 224(14–15), 2771–2785. <https://doi.org/10.1140/epjst/e2015-02588-2>
7. Cottone, F., Vocca, H., Gammaitoni, L. (2009). Nonlinear energy harvesting. *Physical Review Letters*, 102, 080601. <https://doi.org/10.1103/PhysRevLett.102.080601>
8. Daqaq, M.F., Masana, R., Erturk, A., Quinn, D.D. (2014). On the role of nonlinearities in vibratory energy harvesting: A critical review and discussion. *Applied Mechanics Reviews*, 66(4), 040801. <https://doi.org/10.1115/1.4026278>
9. Derkacz, A.J., Dudziak, A. (2021). Savings and investment decisions in the Polish energy Sector. *Sustainability*, 13(2), 553. <https://doi.org/10.3390/>

su13020553

10. Đurin, B., Raič, M., Sušilović, P. (2022). Application of the RAPS method of time series analysis to the assessment of grout curtain performance in Karst—A case study of the hydro energy power plant (HEPP) Mostar Dam in Bosnia and Herzegovina. *Hydrology*, 9(11), 192. <https://doi.org/10.3390/hydrology9110192>
11. Erturk, A., Hoffmann, J., Inman, D.J. (2009). A piezomagnetoelastic structure for broadband vibration energy harvesting. *Applied Physics Letters*, 94, 254102. <https://doi.org/10.1063/1.3159815>
12. Farghali, M., Osman, A.I., Mohamed, I.M.A., Chen, Z., Chen, L., Ihara, I., Yap, P.S., & Rooney, D.W. (2023). Strategies to save energy in the context of the energy crisis: A review. *Environmental Chemistry Letters*, 21(4), 2003–2039. <https://doi.org/10.1007/s10311-023-01591-5>
13. Friswell, M.I., Ali, S.F., Adhikari, S., Lees, A.W., Bilgen, O., Litak, G. (2012). Nonlinear piezoelectric vibration energy harvesting from a vertical cantilever beam with tip mass. *Journal of Intelligent Material Systems and Structures*, 23(13), 1505–1521. <https://doi.org/10.1177/1045389X12455722>
14. Ghazouani, N., Labiadh, M.T., Alassaf, Y., Rezgui, A., & Rajendran, S. (2025). Monitoring and assessment of sand encroachment near Sakala solar farm – Results from field observations. *Journal of Ecological Engineering*, 26(1), 83–94. <https://doi.org/10.12911/22998993/195264>
15. Gis, W., Pielecha, J., Waškiewicz, J., Gis, M., & Menes, M. (2016). Use of certain alternative fuels in road transport in Poland. *IOP Conference Series: Materials Science and Engineering*, 148, 012040. [10.1088/1757-899X/148/1/012040](https://doi.org/10.1088/1757-899X/148/1/012040)
16. Gnap, J., Šarkan, B., Konečný, V., & Skrúcaný, T. (2020). The impact of road transport on the environment. *Lecture Notes in Networks and Systems*, 124, 251–309. https://doi.org/10.1007/978-3-030-42323-0_5
17. Hurtova, I., Sejkorova, M., Verner, J., & Sarkan, B. (2018). Comparison of electricity and fossil fuel consumption in trolleybuses and buses. *Engineering for Rural Development*, 17, 2079–2084. [10.22616/ERDev2018.17.N342](https://doi.org/10.22616/ERDev2018.17.N342)
18. Irawan, Y.H., Raza, S.A., Chern, M.J. (2023). Vortex-induced vibration of two circular cylinders in a side-by-side arrangement at moderate Reynolds number: A numerical study. *Physics of Fluids*, 35, 055126. <https://doi.org/10.1063/5.0139301>
19. Jadoon, T.R., Ali, M.K., Hussain, S., Wasim, A., Jahanzaib, M. (2020). Sustaining power production in hydropower stations of developing countries. *Sustainable Energy Technologies and Assessments*, 37, 100637. <https://doi.org/10.1016/j.seta.2020.100637>
20. Jereb, B., Stopka, O., Skrúcaný, T. (2021). Methodology for estimating the effect of traffic flow management on fuel consumption and CO₂ production: A case study of Celje, Slovenia. *Energies*, 14(6), en14061673. <https://doi.org/10.3390/en14061673>
21. Kantová, N.Č., Sládek, S., Jandačka, J., Čaja, A., Nosek, R. (2021). Simulation of biomass combustion with modified flue gas tract. *Applied Sciences*, 11, 1278. <https://doi.org/10.3390/app11031278>
22. Kettle, J., Aghaei, M., Ahmad, S., Fairbrother, A., Irvine, S., Jacobsson, T.J., Kazim, S., Kazukauskas, V., Lamb, D., Lobato, K. (2022). Review of technology specific degradation in c-Si, CdTe, CIGS, dye sensitised, organic and perovskite solar cells in photovoltaic modules: Understanding how reliability improvements in mature technologies can enhance emerging technologies. *Progress in Photovoltaics: Research and Applications*, 30, 1365–1392. <https://doi.org/10.1002/pip.3577>
23. Kilikevičienė, K., Matijošius, J., Fursenko, A., Kilikevičius, A. (2019). Tests of hail simulation and research of the resulting impact on the structural reliability of solar cells. *Eksplatacija i Niezawodnosc – Maintenance and Reliability*, 21(2), 275–281. <http://dx.doi.org/10.17531/ein.2019.2.12>
24. Ma, X., Gong, L., Pang, Q., Wu, Y., Liu, C., & Wu, Y. (2018). Analysis of the influence of mass block position on the power generation performance of piezoelectric cantilever beam. *Yadian Yu Shengguang/Piezoelectrics and Acoustooptics*, 40(5), 789–792.
25. Ma X & Zhou S. (2022). A review of flow-induced vibration energy harvesters. *Energy Conversion and Management*, 254, 115223. <https://doi.org/10.1016/j.enconman.2022.115223>
26. Małek, A., Karowicz, R., Józwick, K. (2023). A review of technologies in the area of production, storage and use of hydrogen in the automotive industry. *Archives of Automotive Engineering*, 102(4), 41–67. <https://doi.org/10.14669/AM/177038>
27. Michael, E., Tjahjana, D.D.P., & Prabowo, A.R. (2021). Estimating the potential of wind energy resources using Weibull parameters: A case study of the coastline region of Dar es Salaam, Tanzania. *Open Engineering*, 11, 1093–1104. <https://doi.org/10.1515/eng-2021-0108>
28. Mitcheson, P.D., Yeatman, E.M., Rao, G.K., Holmes, A.S., Green, T.C. (2008). Energy harvesting from human and machine motion for wireless electronic devices. *Proceedings of the IEEE*, 96, 1457–1486. doi: 10.1109/JPROC.2008.927494.
29. Munir, A., Zhao, M., Wu, H. (2017). Vortex-induced vibration of two side-by-side cylinders with a small gap in uniform flow. *ASME 2017 36th International Conference on Ocean, Offshore and Arctic Engineering*, June 25–30, 2017, Trondheim, Norway, vol. 2, V002T08A009. <https://doi.org/10.1115/>

OMAE2017-61178

30. Norhafana, M., Noor, M.M., Hairuddin, A.A., Hagos, F.Y., Ayob, S.I., Kadirgama, K., Ramasamy, D. (2019). An experimental study of the performance and emission characteristics of a compression ignition (CI) engine fuelled with palm oil based biodiesel. *AIP Conference Proceedings*, 2059, 020036. <https://doi.org/10.1063/1.5085979>
31. Nowak, R., Pietrzakowski, M. (2016). Experimental and simulation investigations of the cantilever beam energy harvester. *Solid State Phenomena*, 248, 249–255. <https://doi.org/10.4028/www.scientific.net/SSP.248.249>
32. Piotrowska, K., Piasecka, I., Kłos, Z., Marczuk, A., Kasner, R. (2022). Assessment of the life cycle of a wind and photovoltaic power plant in the context of sustainable development of energy systems. *Materials*, 15, 7778. <https://doi.org/10.3390/ma15217778>
33. Szyszlak-Bargłowicz, J., Zajac, G., Kuranc, A., Słowik, T., Dudziak, A., Stoma, M., Wasilewski, J. (2018). Chemical properties of selected agri-food industry waste products in the aspect of their use for energetics purposes. *Przemysł Chemiczny*, 97(5), 779–783.
34. Thapa, S., Magee, T., Zagona, E. (2022). factors that affect hydropower flexibility. *Water*, 14(16), 2563. <https://doi.org/10.3390/w14162563>
35. Trnka, J., Holubčík, M., Kantová, N.Č., Jandačka, J. (2021). Energy performance of a rotary burner using pellets prepared from various alternative biomass residues. *BioResources*, 16, 6737–6749. 10.15376/biores.16.4.6737-6749
36. Wang, J., Gu, S., Zhang, C., Hu, G., Chen, G., Yang, K., Li, H., Lai, Y., Litak, G., Yurchenko, D. (2020). Hybrid wind energy scavenging by coupling vortex-induced vibrations and galloping, *Energy Conversion and Management*, 213, 112835. <https://doi.org/10.1016/j.enconman.2020.112835>
37. Weilin, C., Chunning, J., Dong, X. (2019). Vortex-induced vibrations of two side-by-side circular cylinders with two degrees of freedom in laminar cross-flow. *Computers & Fluids*, 193, 104288. <https://doi.org/10.1016/j.compfluid.2019.104288>
38. White, N.M., Glynne-Jones, P., Beeby, S.P. (2001). A novel thick-film piezoelectric micro-generator. *Smart Materials and Structures*, 10, 850–852. 10.1088/0964-1726/10/4/403
39. Yang, Z., Zhou, S., Zu, J., Inman, D. (2018). High-performance piezoelectric energy harvesters and their applications. *Joule*, 2, 642–697. <https://doi.org/10.1016/j.joule.2018.03.011>
40. Yu, R., Feng, S., Sun, O., Xu, H., Jiang, O., Guo, J., Dai, B., Cui, D., Wang, K. (2024). Ambient energy harvesters in wearable electronics: fundamentals, methodologies, and applications. *Journal of Nanobiotechnology*, 22, 497. <https://doi.org/10.1186/s12951-024-02774-0>
41. Zhang, L., He, Y., Meng, B., Dai, H., Abdelkefi, A., Wang, L. (2023). Omnidirectional wind piezoelectric energy harvesting, *Journal of Physics D: Applied Physics*, 56, 234003. 10.1088/1361-6463/acc5f4
42. Zhao, M., Cheng, L., Zhou, T. (2013). Numerical simulation of vortex-induced vibration of a square cylinder at a low Reynolds number. *Physics of Fluids*, 25, 023603. <https://doi.org/10.1063/1.4792351>
43. Zhou, S., Cao, J., Litak, G., Lin, J. (2018). Numerical analysis and experimental verification of broadband tristable energy harvesters. *Technisches Messen*, 85, 521. <https://doi.org/10.1515/teme-2017-0076>